

Nonlinear gyrofluid computation of edge localised ideal ballooning modes

Alexander Kendl

*Institut für Ionenphysik und Angewandte Physik, Association Euratom-ÖAW,
Universität Innsbruck, A-6020 Innsbruck, Austria*

Bruce D. Scott

*Max-Planck-Institut für Plasmaphysik,
Euratom Association, D-85748 Garching, Germany*

Tiago Ribeiro

*1) Max-Planck-Institut für Plasmaphysik,
Euratom Association, D-85748 Garching, Germany
2) Instituto de Plasmas e Fusão Nuclear,
EURATOM/IST Association, 1049-001 Lisboa, Portugal*

(Dated: October 25, 2018)

Abstract

Three dimensional electromagnetic gyrofluid simulations of the ideal ballooning mode blowout scenario for tokamak edge localized modes (ELMs) are presented. Special emphasis is placed on energetic diagnosis, examining changes in the growth rate in the linear, overshoot, and decay phases. The saturation process is energy transfer to self generated edge turbulence which exhibits an ion temperature gradient (ITG) mode structure. Convergence in the decay phase is found only if the spectrum reaches the ion gyroradius. The equilibrium is a self consistent background whose evolution is taken into account. Approximately two thirds of the total energy in the edge layer is liberated in the blowout. Parameter dependence with respect to plasma pressure and the ion gyroradius is studied. Despite the violent nature of the short-lived process, the transition to nonlinearity is very similar to that found in generic tokamak edge turbulence.

PACS numbers:

I. INTRODUCTION

Edge localised modes (ELMs) are bursty, quasi-periodic expulsions of energy and particles from the plasma edge in the high-confinement state of toroidal magnetised plasmas [1–3]. ELMs originate from the steep pressure gradient pedestal in the outer closed field line region of a tokamak. A substantial release of magnetic and potential energy, caused by a rapid rise of the rate of momentum transfer through the flux surfaces, leads to enhanced transport and loss of heat and particles into the open scrape-off layer (SOL) field line region. The filamented peak heat fluxes during ELMs on the bounding divertor plates present serious restrictions on the performance of future fusion experiments like ITER [4] and necessitate the development of suitable control techniques [5–7].

ELMs generically have been observed in all divertor tokamaks since the initial discovery of the high-confinement “H-mode” state in the early 1980s [8], while characteristics like frequency and intensity are found to vary widely depending on experimental conditions [9]. Stellarator experiments also are reported to show similar bursty quasi-periodic edge activity in the presence of edge transport barriers [10]. Indication that equilibrium drifts are part of the process has been found by experimental diagnosis of an asymmetry of the energy and particle fluxes on each of the divertor plates and evidence that this is sensitive to the directions of the toroidal current and magnetic field [11–13].

Phenomenologically, edge localised mode events in tokamaks have been compared to solar flare eruptions [14, 15], and, in the cataclysmic variability of observed radiation emanating from the plasma, they may seem to bear also some remote resemblance to the outbursts of pressure-driven dwarf novae [16], although the specific instability mechanisms behind these phenomena are clearly of a substantially different nature.

On the other hand, the nature of ELMs has also not yet been completely clarified, in the sense that there is no first-principles based predictive theory available. A number of characteristically different variations of ELMs have been observed in experiments (e.g. Type I, II or III ELMs) which may actually be caused by different instability mechanisms [17]. “Type III” ELM observations show a remarkable similarity to global bursts found in computations of drift-wave turbulence, where the turbulence generated flows and fluxes are closely tied to the self-consistent equilibrium evolution in the plasma edge [18, 19].

“Type I” ELMs in the experiment specifically show stronger magnetic activity during the

burst and are usually associated with the onset of a magneto-hydrodynamic (MHD) ideal ballooning mode (IBM) instability when a threshold pressure gradient is reached in the steep edge pedestal of an H-mode plasma [17]. The possible role of an additional current driven instability (“peeling-ballooning mode”) for “Type I” ELMs has also received recent interest [20–22].

The ideal ballooning instability with nonlinear phases or aftermath has provided a paradigm for recent and current study of the ELM phenomenon theoretically. Explosive MHD instability and associated critical phenomena have been advanced analytically [14]. Early Braginskii fluid simulations were given in support of this [23]. Large, nonlinear MHD codes have been studying this in more detail, resolving several numerical problems and paying specific attention to the details of the magnetic geometry, with mixed results on the phenomenology of the instability beyond its linear phase [24–28]. Whether or not the ideal ballooning instability or its peeling/ballooning variant is actually responsible for ELMs occurring in experiments (here noting the absence of a demonstrably well-resolved L-to-H mode transition in computations from first principles), the nonlinear phase of this “ideal MHD blowout” or “IBM blowout” phenomenon is of physical interest. The ability of the instability to destroy the edge pedestal layer is undisputed, and the term “blowout” is germane. Typical physical parameters lead to a situation wherein the ideal MHD interchange growth rate is comparable to the parallel Alfvén transit time, one and the same with the basic ideal ballooning criterion. This is fast with respect to MHD but not to microturbulence. Provided they can simultaneously treat global MHD (i.e., the spectrum covers both global and ion gyroradius scales), edge-turbulence computations can also address the phenomenon and are even in a position to treat parts of it which fall outside the paradigm of the MHD model.

Here we present nonlinear gyrofluid computations of IBM blowout events localised to the edge/SOL region of a tokamak plasma, resolved to below the ion gyroradius ρ_i . As in the large MHD models the self-consistent evolution of the equilibrium is not only included but is also an integral part of the dependent variables. An electromagnetic 6-moment gyrofluid model (“GEMR”) for both electrons and ions is used, including an energy-conserving treatment of finite ion Larmor radius effects and higher-moment terms which occur in the toroidal drift [29]. The energetic consistency is a key feature since the reaction of parts of the system such as flows and currents which have low energy content can play a central role in the indirect nature of nonlinear dynamics by serving as transfer channels. Although the

gyrofluid model has a different formulation of nonlinear polarisation (the generalisation of “vorticity” to a two-fluid setting) than a fluid or MHD model, full correspondence in the regime of validity of the latter models has been shown [30]. In this sense the model is a superset of global reduced MHD and electromagnetic microturbulence. The global dynamics is in the reduced MHD regime [31] due to low absolute edge beta values ($\beta = 8\pi p/B^2 \sim 10^{-3}$) but the small scales depend on treating the ion gyroradius to arbitrary order. The model does not assume instabilities to occur at any particular scale, but when they occur the resulting spread of the spectrum is found to reach ρ_i within a few eddy turnover times of the onset of nonlinearity in every case computed.

The work reported herein addressed the following points. The relationship of the MHD dynamics to the ideal threshold is much discussed but in the gyrofluid model several mechanisms of microinstability are also present. The threshold issue is obscured by the existence of ion temperature gradient (ITG) drift instabilities at all beta values, with a smooth transition between them. Nevertheless, varying character in the saturation phases is observed at different values. We also address the issue of possible “rho-star” dependence (here the local rho-star is given by ρ_s/L_T where ρ_s is ρ_i evaluated at $T_i = T_e$ and L_T is the scale length of the T_e profile, both evaluated at the mid-pedestal location in minor radius) which would indicate a role for diamagnetic drifts. The gradient is sufficiently steep that $\rho_s/L_T > L_T/qR$ so that none of these effects can be ordered small. We examine the necessary resolution to obtain converged cases, which gives the spectral range actively involved in nonlinear saturation. The main instability at experimentally relevant beta is the ideal ballooning instability but the main saturation process is energy exchange with broadband electromagnetic drift wave/ITG turbulence which the instability itself generates. Due mostly to this, the results turn out to be outside of both the magneto-hydrodynamic (MHD) and collisional Braginskii paradigms, on which most previous approaches have been based. On the other hand, the GEMR model still uses delta-f equations, so the actual profile phenomenology in the SOL region is not well represented, and as in other work with GEMR we concentrate on the properties of the nonlinear dynamics [32].

Following sections give the details of the GEMR model, a discussion of the physical difference between ITG and MHD dynamics and their relative roles, the methods used to pre-set the axisymmetric equilibrium state so that the computations are done in the absence of axisymmetric oscillations whose decay times can be slower than the IBM rise time, the

computations of the blowout phase itself, and the possibility and limitations of quantitative comparison to experiment.

II. THE GYROFLUID MODEL WITH RADially DEPENDENT AXISYMMETRIC GEOMETRY

The gyrofluid model used herein is given in Ref. [29]. It is based on the original derivations given in Refs. [33, 34], with corrections given as motivated by free energy conservation. An alternative derivation using the conservation laws of the underlying gyrokinetic model is given in Ref. [35]. The equations are normalised to spatial scale a and time scale a/c_s where a is the minor radius and c_s is the reference sound speed given by $c_s^2 = T_e/M_i$, that is, in terms of the electron temperature (in energy units) and ion mass. The main parameters are the drift parameter, electron dynamical beta, and electron collisionality, respectively given by

$$\rho_* = \frac{\rho_s}{a} \quad \beta_e = \frac{4\pi p_e}{B^2} \quad \nu_e = \frac{a}{c_s \tau_e} \quad (1)$$

where c and e are the speed of light and fundamental charge, p_e and τ_e are the pressure and Braginskii collision time [36] of the electrons, and $\rho_s = c_s M_i c / e B$ is the drift scale. Note that if $T_i = T_e$ then $\rho_s = \rho_i$. The reference for M_i is the deuterium mass M_D . For the electrons the physical value of the mass $m_e/M_D = 1/3670$ is always used. With global geometry there is no single magnetic field line connection length, but one with a profile with $2\pi q R_0$ a function of the minor radius coordinate, where R_0 is a constant giving the reference value of the major radius.

A. Species constants and gyrofluid moment equations

Each species z has its own set of gyrofluid moment variable equations, one each for density \tilde{n}_z , parallel velocity $\tilde{u}_{z\parallel}$, parallel and perpendicular temperature $\tilde{T}_{z\parallel}$ and $\tilde{T}_{z\perp}$, and parallel and perpendicular energy components of the parallel heat flux $\tilde{q}_{z\parallel}$ and $\tilde{q}_{z\perp}$. They are coupled to the electrostatic and parallel magnetic potentials $\tilde{\phi}$ and \tilde{A}_{\parallel} through self consistent field equations. The tilde denotes a dependent variable to distinguish from constant parameters. The correspondence of these equations to the Braginskii fluid model is given in Ref. [30]. Each species is characterised by a background charge density, temperature/charge ratio, and

mass/charge ratio, given by the normalised parameters

$$a_z = \frac{Zn_z}{n_e} \quad \tau_z = \frac{T_z}{ZT_e} \quad \mu_z = \frac{M_z}{ZM_i}. \quad (2)$$

For electrons $a_z = \tau_z = -1$ and $\mu_z = -m_e/M_i$. For the main ions $a_z = \mu_z = 1$ while $\tau_z = \tau_i$ is kept as a parameter. For the trace ions $a_z = 0$ is always taken. For hot trace ions τ_z is large while μ_z is still moderate. The species gyroradius ρ_z is given by $(\rho_z/\rho_s)^2 = \mu_z\tau_z$, which is always small for electrons, close to unity for main ions, and can be moderate or large for trace ions. For this study a simplified geometry is taken with $B = 1$ except in curvature terms, so magnetic pumping and shaping effects [37] are neglected. Since dynamics at the electron gyroradius scale are neglected the gyroaveraging effects on \tilde{A}_{\parallel} are not treated.

The moment equations are given by

$$\begin{aligned} \frac{\partial \tilde{n}_z}{\partial t} + \mathbf{u}_E \cdot \nabla \tilde{n}_z + \mathbf{w}_E \cdot \nabla \tilde{T}_{z\perp} + \nabla_{\parallel} \tilde{u}_{z\parallel} \\ = \mathcal{K} \left(\tilde{\phi}_G + \frac{\tilde{\Omega}_G}{2} + \tau_z \frac{\tilde{p}_{z\parallel} + \tilde{p}_{z\perp}}{2} \right) \end{aligned} \quad (3)$$

$$\begin{aligned} \frac{\partial}{\partial t} \left(\beta_e \tilde{A}_{\parallel} + \mu_z \tilde{u}_{z\parallel} \right) + \mu_z \mathbf{u}_E \cdot \nabla \tilde{u}_{z\parallel} + \mu_z \mathbf{w}_E \cdot \nabla \tilde{q}_{z\perp} \\ + \nabla_{\parallel} \left(\tilde{\phi}_G + \tau_z \tilde{p}_{z\parallel} \right) \\ = \mu_z \tau_z \mathcal{K} \left(\frac{4\tilde{u}_{z\parallel} + 2\tilde{q}_{z\parallel} + \tilde{q}_{z\perp}}{2} \right) - R_{ei} \end{aligned} \quad (4)$$

$$\begin{aligned} \frac{1}{2} \frac{\partial \tilde{T}_{z\parallel}}{\partial t} + \frac{1}{2} \mathbf{u}_E \cdot \nabla \tilde{T}_{z\parallel} + \nabla_{\parallel} (\tilde{u}_{z\parallel} + \tilde{q}_{z\parallel}) \\ = \mathcal{K} \left(\frac{\tilde{\phi}_G + \tau_z \tilde{p}_{z\parallel} + 2\tau_z \tilde{T}_{z\parallel}}{2} \right) - S_{\Delta} \end{aligned} \quad (5)$$

$$\begin{aligned} \frac{\partial \tilde{T}_{z\perp}}{\partial t} + \mathbf{u}_E \cdot \nabla \tilde{T}_{z\perp} + \mathbf{w}_E \cdot \nabla (\tilde{n}_z + 2\tilde{T}_{z\perp}) + \nabla_{\parallel} \tilde{q}_{z\perp} \\ = \mathcal{K} \left(\frac{\tilde{\phi}_G + \tilde{\Omega}_G + \tau_z \tilde{p}_{z\perp}}{2} + 3 \frac{\tilde{\Omega}_G + \tau_z \tilde{T}_{z\perp}}{2} \right) \\ + S_{\Delta} \end{aligned} \quad (6)$$

$$\begin{aligned} \mu_z \frac{\partial \tilde{q}_{z\parallel}}{\partial t} + \mu_z a_L (\tilde{q}_{z\parallel}) + \mu_z \mathbf{u}_E \cdot \nabla \tilde{q}_{z\parallel} + \frac{3}{2} \tau_z \nabla_{\parallel} \tilde{T}_{z\parallel} \\ = \mu_z \tau_z \mathcal{K} \left(\frac{3\tilde{u}_{z\parallel} + 8\tilde{q}_{z\parallel}}{2} \right) - K_{\parallel} - K_{\Delta} \end{aligned} \quad (7)$$

$$\begin{aligned}
& \mu_z \frac{\partial \tilde{q}_{z\perp}}{\partial t} + \mu_z a_L(\tilde{q}_{z\perp}) + \mu_z \mathbf{u}_E \cdot \nabla \tilde{q}_{z\perp} \\
& \quad + \mu_z \mathbf{w}_E \cdot \nabla (\tilde{u}_{z\parallel} + 2\tilde{q}_{z\perp}) + \nabla_{\parallel} \left(\tilde{\Omega}_G + \tau_z \tilde{T}_{z\perp} \right) \\
& \quad = \mu_z \tau_z \mathcal{K} \left(\frac{\tilde{u}_{z\parallel} + 6\tilde{q}_{z\perp}}{2} \right) - K_{\perp} + K_{\Delta}
\end{aligned} \tag{8}$$

The linearised pressures are given by

$$\tilde{p}_{z\parallel} = \tilde{n}_z + \tilde{T}_{z\parallel} \quad \tilde{p}_{z\perp} = \tilde{n}_z + \tilde{T}_{z\perp} \tag{9}$$

Collisional dissipation is controlled by a collision parameter ν_z analogous to ν_e and a set of numerical constants for each species,

$$\alpha_z \quad \kappa_z \quad \pi_z \tag{10}$$

which are the thermal force, thermal conductivity, and viscosity coefficients involved in parallel dissipation, with values given by the Braginskii model [36], though that regime is never reached in core turbulence. For electrons these coefficients are 0.71 and 3.2 and 0.73, and for ions they are 0 and 3.9 and 0.96, respectively. The resistive dissipation is given by

$$R_{ei} = \frac{m_e}{M_i} \nu_e \left[0.51 \tilde{J}_{\parallel} + \frac{0.71}{3.2} \left(\tilde{q}_{e\parallel} + \tilde{q}_{e\perp} + 0.71 \tilde{J}_{\parallel} \right) \right] \tag{11}$$

with parallel current given by

$$J_{\parallel} = \sum_z a_z \tilde{u}_{z\parallel} \tag{12}$$

noting that it is the electron heat fluxes that enter R_{ei} and as with $\beta_e \tilde{A}_{\parallel}$ the R_{ei} term enters the parallel motion in the same way for every species. The anisotropy dissipation is given by

$$S_{\Delta} = \frac{\nu_z}{3\pi_z} \left(\tilde{T}_{z\parallel} - \tilde{T}_{z\perp} \right) \tag{13}$$

The thermal conduction components are given by

$$K_{\parallel} = \mu_z \tau_z \nu_z \frac{5/2}{\kappa_z} \left(\tilde{q}_{z\parallel} + 0.6\alpha_z \tilde{J}_{\parallel} \right) \tag{14}$$

$$K_{\perp} = \mu_z \tau_z \nu_z \frac{5/2}{\kappa_z} \left(\tilde{q}_{z\perp} + 0.4\alpha_z \tilde{J}_{\parallel} \right) \tag{15}$$

$$K_{\Delta} = 1.28 \mu_z \tau_z \nu_z \frac{5/2}{\kappa_z} \left(\tilde{q}_{z\parallel} - 1.5\tilde{q}_{z\perp} \right) \tag{16}$$

The Landau damping effects are modeled by

$$a_L = \frac{V_z}{qR_0} (1 - 0.125q^2 R_0^2 \nabla_{\parallel}^2) \quad (17)$$

with thermal velocity V_z given by $V_z^2 = \tau_z/\mu_z$.

The gyroaveraging is done through Padé approximants to operators which would act in Fourier space,

$$\Gamma_1 = \left(1 - \frac{1}{2}\rho_z^2 \nabla_{\perp}^2\right)^{-1} \quad \text{and} \quad \Gamma_2 = \rho_z^2 \frac{\partial \Gamma_1}{\partial \rho_z^2} \quad (18)$$

and then the gyroaveraged potentials are

$$\phi_G = \Gamma_1 \phi \quad \text{and} \quad \Omega_G = \Gamma_2 \phi \quad (19)$$

noting that they are species dependent. The main ExB advection and the FLR correction pieces are given by

$$\mathbf{u}_E \cdot \nabla f = [\phi_G, f] - \nu_{\perp} \nabla_{\perp}^4 f + \nu_{\parallel} \nabla_{\parallel}^2 f \quad (20)$$

$$\mathbf{w}_E \cdot \nabla f = [\tilde{\Omega}_G, f] \quad (21)$$

where the $[,]$ symbols denote the nonlinear bracket defined below, and $\nu_{\perp}, \nu_{\parallel}$ denote the artificial dissipation coefficients. The parallel derivative is given by

$$\nabla_{\parallel} f = \frac{1}{qR_0} \frac{\partial f}{\partial s} - \beta_e [\tilde{A}_{\parallel}, f] \quad (22)$$

The curvature operator is given by

$$\mathcal{K}(f) = -[\log B^2, f] \quad (23)$$

B. Field equations for polarisation and induction

The species are coupled through two equations which give the self consistent response of the field potentials to the evolution of the gyrofluid moment variables. The electrostatic potential is governed by quasineutrality, which sets the total space charge density to zero. The density for each species is given by a part due to the gyrocenters and another due to polarisation, which is what sets ϕ . This polarisation equation is given by

$$\frac{1 - \Gamma_0}{\tau_i} \phi = \sum_z a_z \left[\Gamma_1 \tilde{n}_z + \Gamma_2 \tilde{T}_{z\perp} \right] \quad (24)$$

where

$$\Gamma_0 = (1 - \rho_i^2 \nabla_\perp^2)^{-1} \quad (25)$$

gives the gyroscreening of the main ions. In this version of the model the electron and trace ion contributions to gyroscreening are neglected, due to small m_e and zero a_z , respectively. On the right hand side the electrons and main ions enter with oppositely signed a_z values and again here the trace ions do not enter. This establishes them as a trace species.

In a similar way the trace ions are left out of the induction equation due to the zero a_z , so that

$$-\rho_*^2 \nabla_\perp^2 \tilde{A}_\parallel = \tilde{J}_\parallel \quad \text{and} \quad \tilde{J}_\parallel = \sum_z a_z \tilde{u}_{z\parallel} \quad (26)$$

determines \tilde{A}_\parallel noting the way that the normalisation scales it with respect to ρ_* .

More detail, including energy conservation and the relationship of these equations to it, is given in Refs. [29, 35].

C. Representation of the self consistent magnetic geometry

In these expressions the operators ∇_\perp^2 and $\partial/\partial s$ and the nonlinear brackets are determined by the representation of the geometry that is used.

The magnetic geometry is a simplified representation of an axisymmetric magnetic field using field aligned Hamada coordinates. The field representation is

$$\mathbf{B} = I \nabla \varphi + \nabla \Psi \times \nabla \varphi \quad (27)$$

where φ is the physical toroidal angle about the symmetry axis, Ψ is the magnetic flux function, and $I = I(\Psi)$ is given by the constraint of MHD equilibrium. Without loss of generality one may define magnetic flux coordinates $\{V, \theta, \zeta\}$ with the following properties,

$$B^V = 0 \quad B^\theta = \chi_{,V} \quad B^\zeta = \psi_{,V} \quad (28)$$

where $V = V(\Psi)$ is the volume enclosed by the surface with flux Ψ , then $\chi = \chi(V)$ and $\psi = \psi(V)$ are two further flux functions found, and the subscript denotes the partial derivative with respect to V . The ratio $q = d\psi/d\chi$ is another flux function which gives the pitch of the magnetic field. The angles are cyclic on $[0, 1]$ which determines the coordinate Jacobian

to be unity. Hence the metric tensor g_{ij} satisfies $\det g_{ij} \equiv g = 1$. The function χ is found by the constraint that θ is cyclic on the unit interval

$$\chi_{,V}^{-1} = \oint \frac{d\eta}{\mathbf{B} \cdot \nabla \eta} \quad \text{and} \quad \theta = \chi_{,V} \int \frac{d\eta}{\mathbf{B} \cdot \nabla \eta} \quad (29)$$

where η is a simple cyclic coordinate on the flux surface in the poloidal plane (e.g., path length on the curve, or the physical angle position about the magnetic axis with respect to any branch cut). Then q is found

$$q = \frac{I}{2\pi\chi_{,V}} \left\langle \frac{1}{R^2} \right\rangle \quad (30)$$

where the angle brackets give the flux surface average defined as

$$\left\langle \frac{1}{R^2} \right\rangle = \oint \frac{d\theta}{R^2} = \chi_{,V} \oint \frac{d\eta}{R^2 \mathbf{B} \cdot \nabla \eta} \quad (31)$$

Now, $\psi_{,V} = q\chi_{,V}$ is also defined and the toroidal angle coordinate is given by

$$\zeta = \frac{\varphi}{2\pi} + \frac{I}{2\pi\chi_{,V}} \int d\theta \left(\left\langle \frac{1}{R^2} \right\rangle - \frac{1}{R^2} \right) \quad (32)$$

which completes the prescription.

The field aligning is a one-to-one and onto coordinate transform from $\{V, \theta, \zeta\}$ to $\{x, y, s\}$ given by

$$x = V/a^3 \quad y_k = q\theta - \zeta - \alpha_k(x) \quad s = \theta \quad (33)$$

where a is a reference minor radius and α_k is an arbitrary function of x which is chosen to make the off diagonal perpendicular metric element g_k^{xy} vanish at a particular location. This is called the shifted metric procedure [38]. The point is that at any position in s where perpendicular drifts or ∇_{\perp}^2 is evaluated, the coordinate elements are rectangular, and the information contained in magnetic shear enters only in derivatives in the parallel coordinate. The magnetic field components now satisfy

$$B^x = 0 \quad B_k^y = 0 \quad B^s = \chi_{,V} \quad (34)$$

at all locations in space for any choice of α_k . Hence although the perpendicular coordinate elements are rectangular only for one particular location in s the field aligning is exactly satisfied everywhere.

The coordinate metric elements $g^{ij} = \nabla x^i \cdot \nabla x^j$ are found in the $\{V, \theta, \zeta\}$ representation. Then the grid locations $s = s_k$ are all given their own members of the family of these field aligned coordinates via

$$\alpha_k(V) = q s_k + \int_0^V dV' \frac{q g^{V\theta} - g^{V\zeta}}{g^{VV}} \Big|_{\theta=s_k} \quad (35)$$

Then we have

$$g^{xx} = a^{-6} g^{VV} \quad (36)$$

$$g_k^{xy} = 0 \quad (37)$$

$$g_k^{yy} = q^2 g^{\theta\theta} - 2q g^{\theta\zeta} + g^{\zeta\zeta} \quad (38)$$

$$g^{xs} = a^{-3} g^{V\theta} \quad (39)$$

$$g_k^{ys} = q g^{\theta\theta} - g^{\theta\zeta} \quad (40)$$

$$g^{ss} = g^{\theta\theta} \quad (41)$$

at $s = s_k$. The drift tensor elements are given by

$$\mathbf{F} = \epsilon \cdot \mathbf{B} \quad \text{with} \quad F_{xy} = \chi_{,V} \quad (42)$$

that is, F_{xy} is the only independent, nonvanishing component. We have

$$\nabla f \cdot \frac{c}{B^2} \mathbf{B} \times \nabla \phi \equiv \nabla \phi \cdot \frac{c\mathbf{F}}{B^2} \cdot \nabla f \quad (43)$$

which defines the bracket $[\phi, f]$ for any scalar field quantities ϕ and f . With ϕ the electrostatic potential this gives the ExB advection term, for electrons for which FLR corrections are neglected by taking $\rho_e \rightarrow 0$. For ions this is generalised by the FLR corrections as given above.

For local equations as those used here (nonlinearities kept only in advection and magnetic flutter) the geometry model must be modified to retain free energy conservation by the equations. In particular, any function of x such as a radially varying normalised parameter (such as the temperature/charge ration τ_z) multiplying any of the curvature terms will cause them to fail to conserve free energy. The compressibility is already split away from advection and placed into the curvature terms, so the brackets must retain the properties of incompressible advection. This means that the model for \mathbf{F} which is used must satisfy

$$\mathbf{F} \rightarrow \mathbf{F}_0 \quad \text{with} \quad \nabla \cdot \frac{c\mathbf{F}_0}{B^2} = 0 \quad (44)$$

and to avoid any confusion the curvature terms are written with $\log B^2$, which can be given any spatial dependence. Correspondingly, the MHD version of the continuity equation (neglecting diamagnetic fluxes) has already been manipulated according to

$$\frac{\partial n}{\partial t} + \nabla \cdot n \mathbf{u} = 0 \quad (45)$$

$$\left(\frac{\partial}{\partial t} + \mathbf{u} \cdot \nabla \right) \log n + \nabla \cdot \mathbf{u} = 0 \quad (46)$$

and then terms such as $u_{\parallel} \mathbf{b} \cdot \nabla$ are neglected due to the ordering. The result is the same as the local continuity equation

$$\left(\frac{\partial}{\partial t} + \mathbf{u} \cdot \nabla \right) \tilde{n} + n_0 \nabla \cdot \mathbf{u} = 0 \quad (47)$$

where n_0 is a normalising constant, if we identify the dependent variable \tilde{n}/n_0 with $\log n$. It is important to note that with the self consistent background being evolved this also includes the profile: $\nabla \log n \rightarrow \nabla \tilde{n}$.

The simplified geometry is now defined by its operators. The Laplacian and gyroaveraging operators neglect $\partial/\partial s$. The form in the Ampere's law (which does not involve the gyroradius) is given by

$$\nabla^2 = \frac{\partial}{\partial x} g^{xx} \frac{\partial}{\partial x} + g_k^{yy} \frac{\partial^2}{\partial y_k^2} \quad (48)$$

The form in the gyroaveraging operations and polarisation is given by

$$\nabla_{\perp}^2 = \frac{\partial}{\partial x} \frac{g^{xx}}{B^2} \frac{\partial}{\partial x} + \frac{g_k^{yy}}{B^2} \frac{\partial^2}{\partial y_k^2} \quad (49)$$

The brackets are defined by

$$[f, g] = q[f, g]_{xy} + [f, g]_{xs} - q_{,x}(s - s_k)[f, g]_{ys} \quad (50)$$

for any two scalar fields $\{f, g\}$ with each bracket piece defined by

$$[f, g]_{ij} = \left(\frac{\partial f}{\partial x^i} \frac{\partial g}{\partial x^j} - \frac{\partial g}{\partial x^i} \frac{\partial f}{\partial x^j} \right) \quad (51)$$

with the third piece not used since these are always evaluated at $s = s_k$.

III. MODE CHARACTER: ITG VS. MHD

Nonlinear computations on ideal or peeling ballooning mode ELM scenarios in tokamaks have previously been based on magnetohydrodynamic (MHD) models [22, 26–28], and the

respective codes had largely been tailored towards mode structures expected by linear analysis. Restriction to single-fluid MHD equations including two-fluid correction terms allows computations of large to mesoscale dynamics in realistically shaped 2D tokamak equilibria including X-point geometry crossing the separatrix, due to the lack of a need to use field-aligned coordinates. Recent MHD simulations are able to reproduce spatio-temporal mode structures, divertor footprints and other characteristics with good agreement to experimental diagnostics, in particular for the growth and immediate blowout phase of the finger-like instability [40].

However, as soon as the dynamics becomes nonlinear, the spectrum broadens to include scales normally associated with drift wave dynamics. This turbulence is basically of a drift-Alfvén type with strong edge ITG character (see Ref. [39] for the signatures of the various mode structure types), made more powerful than otherwise by the energetic access to the long-wavelength MHD component. The ITG character results from the steeper logarithmic gradients in both temperature profiles, and the lack of involvement of ion temperature fluctuations in the parallel nonadiabatic response of the electrons. Although edge turbulence of this type (cf. [19]) is strongly suppressed in the H-mode phase and is not initially involved in the instability phase, the experience of edge turbulence becomes relevant as these physical components become involved in all the nonlinear phases of the blowout. The saturation and aftermath of the blowout, which in an experiment carries a large part of the actual transport losses that lead to a degradation of the pedestal, should be expected to involve physics not contained in the MHD model.

Ion temperature gradient (ITG) driven modes and ideal ballooning modes are both essentially caused by the gradient and curvature driven interchange instability and show similar character in their initial linear growth phases. Instability is achieved above their respective critical gradients, determined by the ratio $\eta_i = L_n/L_{Ti} > \eta_c$ between density gradient to ion temperature gradient scale lengths for ITG, and by the ideal MHD ballooning parameter $\alpha_M = qR\nabla\beta > \hat{s}$ for IBM, where \hat{s} is the magnetic shear parameter and η_c is a critical threshold which depends on beta, collisionality, and toroidicity. The principal difference between these modes is the relative role of the parallel Alfvén responses which tend towards enforcement of an adiabatic response in the electrons (parallel force balance, with the electron pressure gradient). This is nonexistent in an MHD model and subdominant generally for an MHD instability. But it constrains the electrons if the α_M parameter is below thresh-

old, still allowing the ITG instability because the adiabatic response does not involve the ions. The ITG instability exists at all α_M values, and furthermore for the edge situation the ITG instability and mode structure transitions smoothly to a drift wave one in a nonlinear setting for $\eta_i \sim 1$. Hence there is actually no finite threshold in values of η_i or α_M for the nonlinear edge situation. Therefore, the existence of a threshold in the experiment is the same as the mechanism which maintains the H-mode, which is not yet well understood. It follows that a gyrofluid model computation of an ELM scenario with enough resolution to allow for ion-gyroradius based dynamics has to face the lack of a simple linear threshold in the parameter space.

The transition from initial (micro-)instabilities to generic edge turbulence was studied in detail in Ref. [41]. As the most unstable linear modes crystallise out of an initial random bath of small-amplitude perturbations, the linear growth rate rises and becomes steady. The maximum value of the instantaneous growth rate of total fluctuation free energy E given by $\Gamma(t) = (1/2E)(\partial E/\partial t)$ may be taken as the maximal linear growth rate. The curve of $\Gamma(t)$ then falls very sharply to zero (over about $10L_\perp/c_s$) as saturation occurs. There is some structural adjustment over the next few $100L_\perp/c_s$ as the spectrum fills out, and then the turbulence is fully developed. But over the adjustment phase the value of Γ is well below its previous maximum. We will use the same diagnostic herein, except that the total ion ExB heat flux Q_i averaged over the computational domain is used instead of E because most of E is represented by the self consistent profiles while Q_i is entirely due to fluctuations.

The IBM ELM blowout scenario is similar to this, initially, except that the instability is not a microinstability. Nevertheless, the scale differs by less than an order of magnitude: the toroidal mode numbers for linear ITG instabilities are in the range of $n = 30 - 100$ while the main ideal ballooning mode is near mode number $n = 10$, on the entire flux surface, for these typical ρ_s/L_\perp values (recall $\rho_s = \rho_i$ for $T_e = T_i$, and the ratio T_i/T_e is not far from unity in experimental cases). The ITG mode numbers are determined by the ion gyroradius and the dimensionless scale ratio L_T/qR , while the MHD values are determined by the width of the pedestal. Since L_T is not larger than about $30\rho_i$ in an H-mode pedestal, these scales are not disparate.

Due to the closeness of the native scales, the IBM instability very quickly transfers energy to the ion gyroradius scale, which is only about two or three steps away in a turbulence cascade which acts at a factor of two at each step. This brings the ITG and drift Alfvén physics

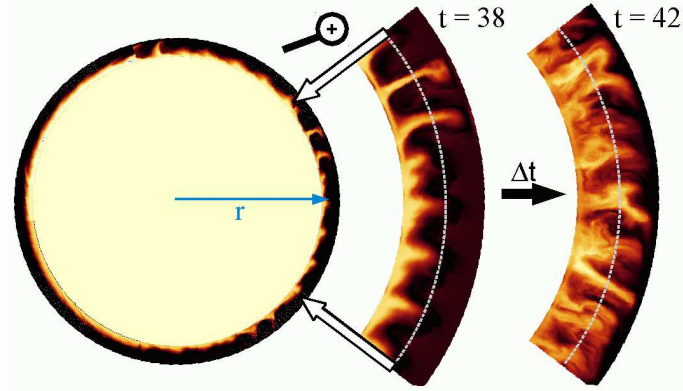


FIG. 1: Visualisation of the tokamak ELM burst: the edge region of a circular poloidal tokamak cross-section is shown on the left with computational perpendicular s -domains ($s = 2, 5, 8, 11, 14$ of $n_s = 16$ total) mapped onto the circle during the maximum growth phase ($t = 38$ in units of a/c_s) of an ideal ballooning mode. On the right, the outer midplane area ($s = 8$ with size $n_x = 48$ and $n_y = 512$) is magnified and the radial domain stretched by a factor of 2 for better visibility at times $t = 38$ (max. flux) and $t = 42$ (turbulent aftermath).

into play, and in any nonlinear stages the latter involves stable shear Alfvén component with substantial energy content. The moment of saturation is defined as the time at which the ion ExB heat flux averaged over the computational domain is maximum; we refer to this as the “peak-flux” time. The results shown below indicate that coincides with the establishment of the fully turbulent regime. Representation of this phase requires resolution of all scales and inclusion of the appropriate drift wave physics in the model. How much resolution is actually needed depends on the strength of the blowout, which is situation dependent. We therefore include a resolution scan on the toroidal mode number spectrum. The result is that convergence is reached in the temporal phases just after peak flux only if the spectrum reaches down to $k_y \rho_i = 1$.

The self-consistent equilibrium coupling in our gyrofluid model only allows treatment of shifted circular $s-\alpha$ geometry (the difference to MHD codes is that the high-resolution FLR-gyrofluid dynamics necessitates field-aligned coordinates). Effects of flux surface shaping are postponed to later studies. Our focus here is on basic physics issues regarding the ability of the model to capture MHD phenomena (see also Ref. [18] concerning global Alfvén oscillations with self consistent profiles), resolution, turbulent character, scalings and tests which are also accessible by $s-\alpha$ geometry. In particular, the theory of explosive instability

has been formulated for circular geometry [14] and is therefore accessible by the present model.

IV. MODELLING OF INITIAL PROFILES

First-principles based local drift wave edge turbulence simulations are not able to obtain a realistic H-mode edge state with the known experimental characteristics: correct density and temperature pedestal profiles shapes or strength of flow shear are not obtained by self-consistent evolution by specifying core sources only, nor has a threshold transition character been found in any verified edge turbulence simulation [19]. Therefore some kind of “modelling” has to take place when the IBM instability (as an H-mode phenomenon) and its subsequent nonlinear evolution is simulated with a nonlinear gyrofluid turbulence code: Although the realistic development of an edge transport barrier (and thus a full ELM cycle) can not be directly obtained, one still may prescribe the H-mode pedestal profile before the onset of an ELM, known from experimental data, as an initial state for the simulation. As a base case for the prescribed pedestal profiles the well diagnosed edge characteristics of ASDEX Upgrade H-mode shot #17151 is used here [42].

The local parameters, taken as mid pedestal values, correspond to electron and ion temperatures $T_e = 300$ eV, $T_i = 360$ eV, densities $n_e = n_i = 2.5 \cdot 10^{19} \text{ m}^{-3}$, magnetic field strength $B = 2.0$ T, major torus radius $R = 1.65$ m, aspect ratio $R/a = 3.3$, perpendicular temperature gradient length $L_T = L_\perp = 3.0$ cm, density gradient length $L_n = 6.0$ cm. The profile of the safety factor $q = 1.5 + 3.5(r/a)^2$ is parabolic yielding local values at the last closed flux surface (LCFS, $r/a = 1.0$) of $q_a = 5.0$ and $\hat{s}_a = 1.4$. The radial domain of the simulations covers a range of L_\perp on either side of the LCFS. The nominal pressure values are $p_e = n_e T_e$ and $p_i = n_i T_i$. All times are given in units of a/c_s .

The computational grid is given in terms of the $\{x, y, s\}$ coordinate domains. The spacing is equidistant. For each grid point in the third coordinate $s = s_k$ the y -coordinate is y_k as defined in Eqs. (33,35) so that for each grid point s_k the coordinate system $y = y_k$ is the one which has $g_k^{xy} = 0$ at $s = s_k$. For the nominal case $n_y = 512$ perpendicular and $n_s = 32$ parallel mesh points are used. The radial domain with $n_x = 64$ spans the plasma edge region between the H-mode pedestal top, with plasma core parameters as inner boundary values, and the outer bounded scrape-off layer region ($r/a = 1 \pm 0.06$). This represents a

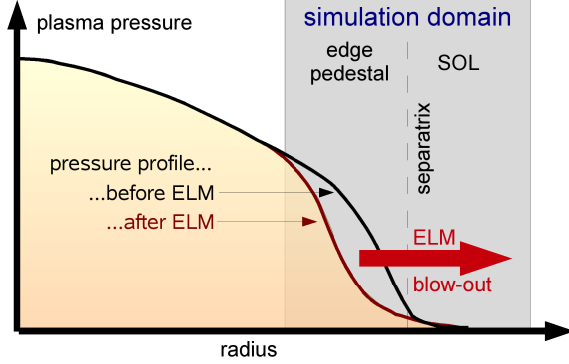


FIG. 2: Radial tokamak edge pedestal profiles of the plasma pressure before and after an ELM blowout event across the separatrix into the scrape-off layer (SOL). The area shaded in grey shows the present radial numerical simulation domain.

spatial range from the global scale to smaller than the ion gyroradius scale, with a ratio $\delta = \rho_s/a = 0.001875$ between ion gyroradius ρ_s and minor torus radius a . In the SOL region ($r > a$) the parallel boundary condition is replaced by a Debye sheath model whose treatment is given in Ref. [44].

V. PROFILE PRE-EQUILIBRATION

The initial conditions are thus prescribed and are based on experimentally diagnosed radial temperature and density pedestal profiles $T(r)$ and $n(r)$ for each species (electrons and ions). A consistent electrostatic potential $\phi(r)$ is derived by numerically solving the neoclassical balances (parallel dynamics, toroidal drifts, and collisional dissipation, but not transport) in a pre-processing step with a modified (zonally frozen) GEMR setup, resulting in a time-steady 2D dissipative solution. The $s - \alpha$ MHD equilibrium in turn is set internally in GEMR by computing the Shafranov shift, and in the present setup would not be consistently described by prescribed in terms of external or coupled shaped equilibrium solvers [18].

The parallel and perpendicular electron and ion temperatures, $T_{e\parallel}$, $T_{e\perp}$, $T_{i\parallel}$ and $T_{i\perp}$, are directly adopted and fixed from experimentally derived values by filtering the zonal component out of the total time derivative $\partial T/\partial t = S_T$. Their values are zonally frozen by setting

$$\frac{\partial T}{\partial t} = S_T - \langle S_T \rangle \quad (52)$$

where $\langle S_T \rangle$ is the zonal (parallel and perpendicular) average of all right-hand-side terms S_T

in the temperature evolution (Eqs. 5,6) including numerical dissipation.

On the other hand, gyrocenter densities n_e and n_i have to be set to obey relaxation relations that allow the vorticity to freely evolve into equilibrium. This is achieved by freezing the zonal component of the sum $n_e + \tau_i n_i$, where $\tau_i = T_i/T_e$, as the density part of the pressure during the equilibration phase, but allowing the difference (i.e., vorticity) to evolve freely. This ensures that the contribution of densities to the total pressure is zonally frozen through the relation

$$\frac{\partial}{\partial t}(n_e + \tau_i n_i) = S_e + \tau_i S_i - \langle S_e + \tau_i S_i \rangle \quad (53)$$

while the densities relax regarding to

$$\frac{\partial n_e}{\partial t} = S_e - \frac{1}{1 + \tau_i} \langle S_e + \tau_i S_i \rangle \quad (54)$$

and

$$\frac{\partial n_i}{\partial t} = S_i - \frac{1}{1 + \tau_i} \langle S_e + \tau_i S_i \rangle \quad (55)$$

The numerical solution of the equilibration phase, starting directly from realistically steep pedestal profiles $T_0(r)$, into steady state is delayed by long, weakly damped global geodesic Alfvén oscillations. Convergence is expedited by ramping up all of the gradients gradually from zero to prescribed value over the first $\Delta t = \tau_r = 50 a/c_s$ of the run by

$$\frac{\partial T}{\partial t} = S_T - \langle S_T \rangle + \frac{1}{\tau_r} T_0(x). \quad (56)$$

This pre-processing equilibration phase is run until convergence with reduced perpendicular resolution $(n_x, n_y, n_z) = (64 \times 4 \times 32)$, and without the ExB and magnetic flutter nonlinearities, which allows establishment of the 2D structure in a smooth manner. Then, the resolution is increased to the nominal values $(64 \times 512 \times 32)$, and a random turbulent bath with relative amplitude $10^{-4} \rho_s/L_\perp$ is added to the background pedestal profiles inside the closed flux surface region. This procedure reduces transient Alfvénic and geodesic acoustic ringing and prepares a reproducible initial state. However, the following sudden release of the nonlinearities also leads to transient oscillations. Depending on parameters, these may still be present at the onset of the instabilities, and can obscure a clean view on the nonlinear growth rates, which will be relevant for the discussion below on diagnosing linear or explosive instability.

A schematic sketch of the equilibrium pedestal profiles, representing an idealised ASDEX Upgrade H-mode scenario [42], is shown in Fig. 2 together with the final relaxed state after the ELM blowout phase (which is discussed in the next section).

VI. COMPUTATION OF THE ELM BLOWOUT

When this initialised pedestal pressure profile is ideal ballooning unstable, the IBM instability in GEMR simulations is observed to be linearly growing in the pedestal region and at the onset of nonlinearity further overshoots and saturates, representing the beginning of the turbulent blowout phase during which a substantial fraction of the pedestal energy is thrown onto the SOL. Subsequent evolution involves turbulence in both the pedestal and SOL regions as the original pedestal energy is dissipated.

Previous nonlinear approaches on ELM ideal ballooning mode burst computations have treated only the initial growth and nonlinear phases, focused on low-wavelength modes and resolved only the MHD-relevant scales, excluding treatment or discussion of the ion gyro-radius scales. This however precludes the development of fully developed microturbulence which is caused by the onset of nonlinearity (robust transfer of free energy to smaller scales). Ultimately, this microturbulence decides both the transition to nonlinearity and the eventual saturation; that is, most of the post-peak transport curve. This affects the MHD scenario of nonlinear explosive growth which most previous work advances. However, we find that the exclusion of the ion gyroradius scales produces an under-resolved situation.

We measure the quantitative character of the growth in both linear and nonlinear phases with a growth curve

$$\Gamma(t) = \frac{1}{2Q_i} \frac{\partial Q_i}{\partial t} \quad (57)$$

defined in terms of the heat flux Q_i instead of the fluctuation free energy as explained above.

The heat flux is computed as a zonal (flux surface) average,

$$Q_i(x) = \oint dy ds \left[(0.5\tilde{p}_{i\parallel} + \tilde{p}_{i\perp})u_E^x + (\tilde{p}_{i\perp} + 2n_i\tilde{T}_{i\perp})w_E^x \right] \quad (58)$$

$$u_E^x = -\frac{cF_0^{xy}}{B^2} \frac{\partial \phi_G}{\partial y} \quad w_E^x = -\frac{cF_0^{xy}}{B^2} \frac{\partial \Omega_G}{\partial y} \quad (59)$$

and then the time trace $Q_i(t)$, normalised in terms of $p_e c_s$ at nominal parameters, is computed as a volume average over the central half of the radial domain.

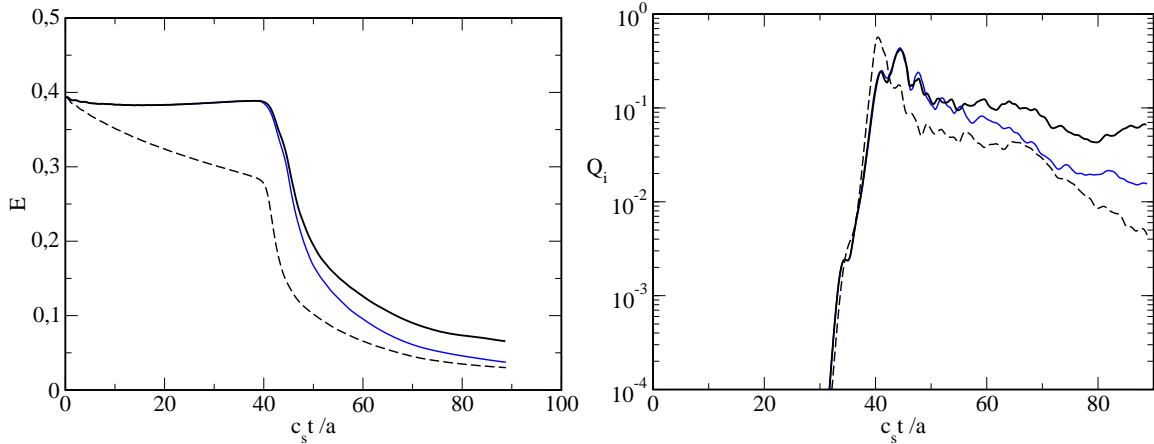


FIG. 3: Total energy $E(t)$ (top figure) and ion heat flux $Q_i(t)$ (bottom figure) during the ELM blowout: without source maintenance (dashed curve); with the source term switched off at the time of maximum instability (here: at $t = 40$); and with the source maintained for the whole simulation time.

The IBM instability, which follows the random seeding of the pre-processed pedestal profile in our computations, is very violent, growing for the nominal case at a rate $\Gamma = 0.18c_s/L_\perp$, just below the ideal interchange rate. On the other hand the growth curve $\Gamma(t)$ appears qualitatively the same as in basic turbulence cases. At all time points in the nonlinear phase $\Gamma(t)$ is well below its previous maximum. Just after initial saturation there is some nonlinear evolution in which $\Gamma(t)$ crosses zero before settling down into long-term statistical saturation. At late times the initial blowout no longer imprints the results: with a fixed source one merely finds bursty turbulence thereafter. Hence, there is no evidence for explosive instability in this nominal case, which, if present, would be visible in a finite time singularity in the fluctuating free energy $E \sim (\delta f)^2 \sim (t - t_{crit})^{-p}$ rising with a power p .

The burst and the resulting decaying turbulence act to transport the pedestal plasma across the LCFS, where energy and particles are lost within short times by parallel boundary outflow to the scrape-off layer (SOL) limiter. Without maintenance of a heat and particle source at the core boundary, this leads to decay of the initial gradient with a rapid onset at the initial transition to nonlinearity at about $t = 40$. This time point also corresponds to the peak-flux time.

However, the ion temperature profile already starts decaying during the low-amplitude linear growth phase, due to neoclassical (finite Larmor radius) transport (for detail on how

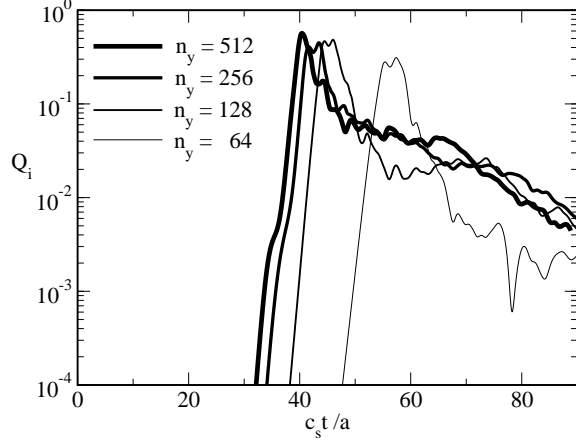


FIG. 4: Consistency check for different perpendicular resolutions by varying the grid point number n_y between 64 and 512. Convergence is seen for $n_y = 256$ and higher.

this works in a fluid model see Ref. [43]). This situation is shown in Fig. 3 (left frame, dashed line), where the total pedestal energy is reduced by a quarter of its initial content before the peak flux phase. Therefore we test sensitivity against sources. Maintenance of the ion temperature profile by a fixed ion heat source localised to the inner boundary (following the method for driven cases in Ref. [45]) ensures nearly unchanged gradients during the linear growth phase. At the end of the simulation time ($t = 90$) after the ELM burst, the energy content is reduced to around 10% of the initial content when the source is absent or is switched off at the peak flux time ($t = 40$), and to around 20% when the source is maintained for the whole simulation time.

The influence of either switching off the source or maintaining the zonal profiles on the nonlinear ion heat flux $Q_i(t)$ is shown in Fig. 3 (right): the linear growth phase and the peak flux is not significantly changed by the source. As expected, the heat flux saturates for late times with maintained core boundary inflow and is otherwise decaying.

Consistency checks on the perpendicular resolution are made by varying n_y between 64, 128, 256 and 512. The evolution of $Q_i(t)$ for these cases is shown in Fig. 4. The $n_y = 64$ case is clearly under-resolved and overestimates the total energy decay by a factor 2. For $n_y = 128$ the initial part of the post-peak decay phase disagrees with the $n_y = 512$ case. Convergence is found for $n_y = 256$ and higher. The nonlinear saturation phase thus requires resolving the ion gyroradius scale. This is the clearest indication that turbulence for toroidal mode numbers beyond about 30 extending down to the $k_y \rho_i \sim 1$ range is involved in the

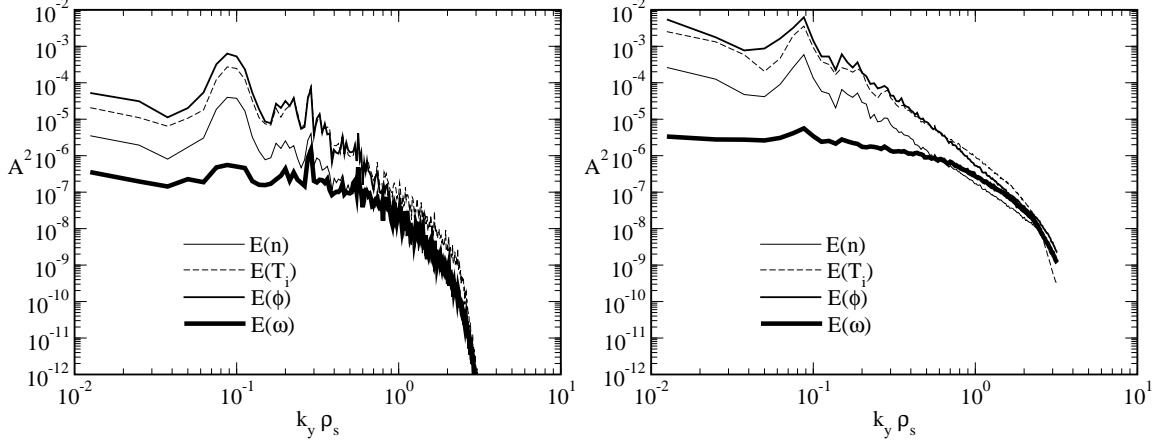


FIG. 5: Perpendicular mode number $k_y \rho_s$ spectra for $t = 38$ (top) and $t = 42$ (bottom) around the peak flux phase. The vorticity spectrum (bold lines) is already flattening down to the ion gyroradius scale for $t = 42$ only a few μs after the maximum linear growth phase.

blowout saturation process.

The transition from linear instability to turbulence is studied during the peak flux phase around $t = 40$. Fig. 5 shows perpendicular mode number $k_y \rho_s$ spectra of the squared amplitude of various fluctuating plasma quantities (density n , ion temperature T_i , electrostatic potential ϕ and vorticity ω) for $t = 38$ and $t = 42$. This time difference corresponds to $\Delta t = 15 \mu s$ in physical units and around $70 L_{\perp} / c_s$ in local drift units, which is only slightly faster than the overshoot and saturation times known from edge microinstability cases [41]. Initially, the ion temperature gradient (ITG) driven microinstability and the ideal ballooning mode (IBM) compete in growth out of the random low-amplitude bath. The ITG mode grows strongest near the separatrix due to radially local steepening by parallel SOL diffusion, which in our simulations may be overestimated by using the standard fluid Bohm outflow boundary conditions. For $t = 38$ the linear IBM is clearly dominant near a toroidal mode number of 9-10 for the nominal AUG parameters, consistent with experimental observations [46]. Around $t = 42$ rapid formation of a turbulent cascade range in the spectra is observed and the vorticity spectrum is already spread out to the ion gyroradius scale ($k_y \rho_s = 1$). This is a manifestation of the role of self generated drift wave turbulence in the saturation process. Because of the way both the diffusive mixing and vorticity scattering nonlinearities enter the drift wave physics [39] the spectrum is held together as a unit, all scales down to ρ_i are involved in the saturation phase of the overall ELM blowout transport. The involvement

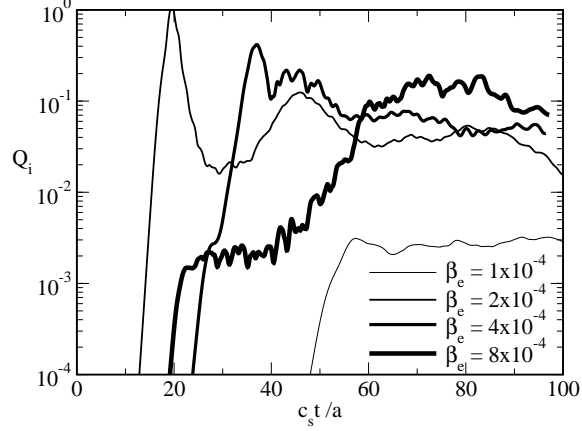


FIG. 6: Competing growth of ITG, microtearing and IBM instabilities determine onset times and intensities of the blowout time traces $Q_i(t)$ when scaling with the local plasma beta: for $\beta_e = 10^{-4}$ only an ITG micro-instability is growing around $t = 50$ and saturating on a low H-mode transport level. For $\beta_e = 2 \cdot 10^{-4}$ the IBM instability dominates and leads to a clean ELM signal around $t = 20$. In the nominal case ($\beta_e = 2 \cdot 10^{-4}$) ITG and IBM MHD growth compete initially with similar growth rates but the ideal ballooning mode takes over around $t = 30$ and further determines the blowout. For $\beta_e = 8 \cdot 10^{-4}$ a microtearing instability is saturating on a gyro-Bohm transport level around $t = 20$ and is transformed into more violent ITG MHD turbulence after deterioration of the initial electron temperature gradient ($t > 50$).

of ρ_i at unit order, in turn, necessitates a nonlinear gyrofluid model (and at some later date, a nonlinear gyrokinetic model).

The characteristics of the blowout at various plasma beta is studied for $0.5 \cdot 10^{-4} < \beta_e < 8 \cdot 10^{-4}$, with the absolute β a factor of 4.8 higher due to the $T_i/T_e = 1.2$ value. A competition between unstable growth of ITG high-n modes and IBM low-n modes is observed: For low β an early onset of ITG turbulence degenerates the profile and influences the strength of the IBM. For large β the nonlinear saturation is acting faster and stronger. The two effects lead to a rather nondistinctive result concerning the peak ELM flux as shown in Fig. 6, with a continuous transition between ITG and IBM triggered onset of the turbulent aftermath.

The presence or absence of background current gradient terms, which in this model are set by replacing ($\tilde{J}_{\parallel} \rightarrow \tilde{J}_{\parallel} + J_0$) everywhere the electron parallel velocity \tilde{v}_{\parallel} appears in the equations, with J_0 given by the q profile, was found to have no discernible effect on the result. Indeed self-consistent inclusion of ∇J_0 effects with possible role in the L-to-H

transition was among the motivations of the GEMR model in the first place [18]. However, the magnitude of even an impressive pedestal current peak is only one to three times the nominal saturation current given by $n_e e c_s$, while values closer to $n_e e c_s qR/L_\perp$ are required to enter the energetics effectively. Since $qR/L_\perp \sim 200$ for the nominal case, current gradient effects are very weak.

VII. CONCLUSIONS

The main conclusion of this study is that the qualitative nature of the saturation and aftermath of the initial IBM blowout is the same as for generic edge turbulence given a small-amplitude start. The transition from linear mode structure and energetics to turbulence found for these blowout cases is the same as in Ref. [41]. Only the nature of the linear mode itself differs. The blowout saturates upon its own self generated drift-Alfvén turbulence, with a strong ion temperature component given the gradients. The vorticity spectrum reaches quickly to the ion gyroradius (ρ_i) scale, requiring the gyrofluid model and explaining the numerical difficulties seen with Braginskii models — it can be argued that the cases given in Ref. [23] crash on entry to the nonlinear stage. Convergence in the aftermath requires resolving at least ρ_i . Unfortunately, due to the lack of a self consistent H-mode state in a well resolved computation, no threshold is found. At lower beta values one simply finds generic edge turbulence driven by the temperature gradients. It is not clear that this scenario really describes an actual ELM, although the energetic growth and decay curves are not unrealistic. However, with a well resolved transition to nonlinearity in both the energetic peak and aftermath phases, our studies find no evidence of an explosive MHD phenomenology. Indeed it can be argued that nonlinear MHD processes are pre-empted by the efficient transfer to smaller scales through the two-fluid drift wave physics more commonly associated with microturbulence.

Acknowledgements

This work was supported by the Austrian Science Fund FWF under contract Y398, by a junior research grant (“Nachwuchsförderung”) from University of Innsbruck, and by the European Communities under the Contract of Associations between Euratom and the

Austrian Academy of Sciences, carried out within the framework of the European Fusion Development Agreement. The views and opinions herein do not necessarily reflect those of the European Commission.

- [1] H. Zohm, Plasma Phys. Control. Fusion **38**, 105 (1996).
- [2] J.W. Connor, Plasma Phys. Control. Fusion **40**, 531 (1998).
- [3] M. Becoulet, G. Huysmans, Y. Sarazin et al., Plasma Phys. Control. Fusion **45**, A93 (2003).
- [4] K. Ikeda et al., Nucl. Fusion **47**, E01 (2007).
- [5] P.T. Lang, J. Neuhauser, L.D. Horton et al., Nucl. Fusion **43**, 1110 (2003).
- [6] T.E. Evans, R.A. Moyer, K.H. Burrell et al., Nature Physics **2**, 419 (2006).
- [7] E. Hand, Nature **452**, 11 (2008).
- [8] F. Wagner, G. Becker, K. Behringer et al., Phys. Rev. Lett. **49**, 1408 (1982).
- [9] K. Kamiya, N. Asakura, J. Boedo et al., Plasma Phys. Control. Fusion **49**, S43 (2007).
- [10] V. Erckmann, F. Wagner, J. Baldzuhn et al., Phys. Rev. Lett. **70**, 2086 (1993).
- [11] T. Eich, A. Herrmann, J. Neuhauser et al., Phys. Rev. Lett. **91**, 195003 (2003).
- [12] T. Eich, A. Kallenbach, R.A. Pitts et al., J. Nucl. Materials **363-365**, 989 (2007).
- [13] T. Eich, A. Kallenbach, W. Fundamenski et al., J. Nucl. Materials **390-391**, 760 (2009).
- [14] H.R. Wilson and S.C. Cowley, Phys. Rev. Lett. **92**, 175006 (2004).
- [15] W. Fundamenski, V. Naulin, T. Neukirch et al., Plasma Phys. Control. Fusion **49**, R43 (2007).
- [16] G.T. Bath, Rep. Prog. Phys **48**, 483 (1985).
- [17] J.W. Connor, Plasma Phys. Control. Fusion **40**, 191 (1998).
- [18] B.D. Scott, Contrib. Plasma Phys. **46**, 714 (2006).
- [19] B.D. Scott, Plasma Phys. Control. Fusion **49**, S25 (2007).
- [20] P. Snyder, H. Wilson, J. Ferron, et al. Phys. Plasmas **9**, 2037 (2002).
- [21] H. Wilson, S. Cowley, A. Kirk, P. Snyder Plasma Phys. Control. Fusion **48** A71 (2006).
- [22] P.B. Snyder, K.H. Burrell, H.R. Wilson, et al. Nucl. Fusion **47**, 961 (2007).
- [23] P. Snyder, H. Wilson, X. Xu Phys. Plasmas **12**, 056115 (2005)
- [24] D.P. Brennan, S.E. Kruger, D.D. Schnack, C.R. Sovinec, A. Pankin, J. Phys. Conf. Series **46**, 63 (2006).
- [25] H. Strauss, L. Sugiyama L., C.S. Chang, et al. Proc. 21st IAEA Fusion En-

- ergy Conf. (Chengdu, China, 2006) (Vienna: IAEA) CD-ROM file TH/P8-6 and <http://www-naweb.iaea.org/napc/physics/FEC/FEC2006/html/index.htm>
- [26] A.Y. Pankin, G. Bateman, D.P. Brennan, A.H. Kritiz, S. Kruger, P.B. Snyder, C. Sovinec and the NIMROD team, *Plasma Phys. Control. Fusion* **49**, S63 (2007).
 - [27] N. Mizuguchi, R. Khan, T. Hayashi and N. Nakajima *Nucl. Fusion* **47**, 579 (2007)
 - [28] G.T.A. Huysmans and O. Czarny, *Nucl. Fusion* **47**, 659 (2007).
 - [29] B.D. Scott, *Phys. Plasmas* **12**, 102307 (2005).
 - [30] B.D. Scott, *Phys. Plasmas* **14**, 102318 (2007).
 - [31] H. Strauss, *Phys. Fluids* **19**, 134 (1976).
 - [32] S. Zweben, B. Scott, J. Terry et al., *Phys. Plasmas* **16**, 082505 (2009).
 - [33] W. Dorland and G. Hammett, *Phys. Fluids B* **5**, 812 (1993).
 - [34] M. A. Beer and G. Hammett, *Phys. Plasmas* **3**, 4046 (1996).
 - [35] B.D. Scott, Derivation via free energy conservation constraints of gyrofluid equations with finite-gyroradius electromagnetic nonlinearities, submitted to *Phys. Plasmas*, arXiv:0710.4899 (2007).
 - [36] S.I. Braginskii, *Rev. Plasma Phys.* **1**, 205 (1965).
 - [37] A. Kendl and B.D. Scott, *Phys. Plasmas* **13**, 012504 (2006).
 - [38] B.D. Scott, *Phys. Plasmas* **8**, 447 (2001).
 - [39] B.D. Scott, *New Journal of Physics* **4**, 52 (2002).
 - [40] G.T.A. Huysmans, submitted to *Plasma Phys. Control. Fusion* **51**, (2009).
 - [41] B.D. Scott, *Phys. Plasmas* **12**, 062314 (2005).
 - [42] L.D. Horton, A.V. Chankin, Y.P. Chen et al., *Nucl. Fusion* **45**, 856 (2005).
 - [43] G. L. Falchetto, M. Ottaviani, X. Garbet, and A. Smolyakov, *Phys. Plasmas* **14**, 082304 (2007).
 - [44] T. Ribeiro and B. Scott, *Plasma Phys. Control. Fusion* **50**, 055007 (2008).
 - [45] B.D. Scott, *Phys. Plasmas* **12**, 082305 (2005).
 - [46] B. Kurzan, H.D. Murmann, J. Neuhauser, *Phys. Rev. Lett.* **95**, 145001 (2005).